

Cite this article as: Zhao Changyu, Liu Ying, Zhao Wei, et al. Effect of Low-Pressure Sintering on Microstructure and Service Stability of NdFeB Magnets[J]. Rare Metal Materials and Engineering, 2023, 52(01): 74-80.

ARTICLE

Effect of Low-Pressure Sintering on Microstructure and Service Stability of NdFeB Magnets

Zhao Changyu, Liu Ying, Zhao Wei, Hou Henan, Li Jun

College of Materials Science and Engineering, Sichuan University, Chengdu 610065, China

Abstract: The internal relationship between the microstructure and service stability of NdFeB magnets was investigated. Results show that the NdFeB magnets after low-pressure sintering have significantly finer grains and more uniform distribution of the Nd-rich phase among the grains, which is beneficial to obtain smaller coercivity temperature coefficients of magnets, thereby improving the temperature stability. Compared with that of the magnets after vacuum sintering, the coercivity temperature coefficient of low-pressure-sintered magnets is reduced from $-0.488\%/^{\circ}\text{C}$ to $-0.472\%/^{\circ}\text{C}$. However, the flow of the Nd-rich phase from the triangular grain boundary to the main phase intergranular area promotes the formation of complete network structure, which degrades the corrosion resistance of the magnets. The low-pressure-sintered magnets show more serious corrosion mass loss after immersion in 3.5wt% NaCl solution, presenting a stronger corrosion tendency.

Key words: low-pressure-sintered NdFeB magnet; microstructure; temperature stability; corrosion resistance

Permanent magnets based on the sintered neodymium-iron-boron (Nd-Fe-B) alloys are widely applied in the fields of motor, generator, and audiovisual equipment due to their excellent magnetic properties^[1-2]. Over the past decade, higher demands for high-performance permanent magnets are raised^[3]. The magnetic properties of sintered Nd-Fe-B magnets have been widely researched, but their working stability is rarely reported. Sintered magnets usually serve in the humid and high-temperature environment, which requires outstanding service stability in order to satisfy the long-term stable performance.

The service stability of sintered magnets usually includes thermal stability and corrosion resistance. Traditionally, alloying elements, such as Co and Ga, are doped into the substrate material to improve the thermal stability of the magnets^[4-5]. However, the superb coercivity cannot remain and the preparation cost is high. It is found that the intergranular diffusion of heavy rare earth elements can improve the thermal stability, because of the core-shell structure formed at the edges of crystal grains^[6-8]. Not only coercivity, but also the coercivity temperature coefficient β_{Hc} is sensitive to the alloy microstructure^[9-10]. Besides, adding Co

and Cu can improve the corrosion resistance of sintered magnets^[11-13]. However, the magnetic properties will degrade and the preparation cost is high. Li et al^[14] found that compared with the sintered magnets, the hot-deformed magnets have outstanding corrosion resistance because of their brick-like structure. It can be inferred that the microstructure of the magnets can also affect the corrosion resistance. Therefore, the optimization of thermal stability and corrosion resistance can be achieved via the microstructure control. Zhao et al^[15] reported a novel sintering method for magnets to obtain the specific microstructure by introducing pressure without changing the alloy composition. The effect of microstructure changes on the long-term service stability of magnets is rarely reported. Therefore, the evolution of the long-term stability of magnets with different microstructures was investigated in this research. The internal mechanism was discussed, providing references for the design and production of magnets.

1 Experiment

Sintered commercial N48SH magnets with the nominal composition of $(\text{Pr}, \text{Nd})_{30.4}\text{Ho}_{0.3}\text{Fe}_{66.14}\text{B}_{1.0}\text{M}_{2.16}$ (wt%, $M=\text{Al}, \text{Cu}$,

Received date: March 07, 2022

Foundation item: Sichuan Province Key Technology and Development Program of Panxi Experimental Area (2018KJT0040); Sichuan University Engineering Common Discipline Project (2020SCUNG201)

Corresponding author: Li Jun, Ph. D., Professor, College of Materials Science and Engineering, Sichuan University, Chengdu 610065, P. R. China, E-mail: abthonyli@163.com

Copyright © 2023, Northwest Institute for Nonferrous Metal Research. Published by Science Press. All rights reserved.

Nb, Ga, Co) were prepared by powder metallurgy. The magnets were separately prepared by the low-pressure sintering^[15] and the traditional vacuum sintering. Different magnet specimens were cut by the wire electrical discharge machining. Then the specimen surface was polished by sandpaper and diamond paste for observation and analysis. The initial morphology was observed by scanning electron microscope (SEM, JSM-7900F). Two hundred grains were randomly selected, and the grain size was measured by Nano Measurer software. In addition, five regions were randomly selected, and the ratio of the bulk Nd-rich phase area to the overall area was calculated by Image-Pro Plus software. The magnetic performance at different temperatures was characterized by the physical property measurement system (PPMS-9). The temperature coefficient of remanence α_{B_r} and that of coercivity $\beta_{H_{cj}}$ can be calculated by Eq.(1) and Eq.(2), respectively, as follows:

$$\alpha_{B_r} = \frac{B_r(T_1) - B_r(T_0)}{B_r(T_0)(T_1 - T_0)} \times 100\% \quad (1)$$

$$\beta_{H_{cj}} = \frac{H_{cj}(T_1) - H_{cj}(T_0)}{H_{cj}(T_0)(T_1 - T_0)} \times 100\% \quad (2)$$

where B_r is the remanence; H_{cj} is the coercivity; T_0 is the starting temperature; T_1 is the actual test temperature.

After immersion in 3.5wt% NaCl solution for different durations, the corrosion products were ultrasonically removed from the magnet specimen by deionized water and then the specimen was dried in a vacuum oven. Mass change before and after corrosion was characterized by Analytical balance (ATX-224). SEM equipped with energy dispersive spectrometer (EDS, Ultima Max 65) was used for the microstructure characterization of the magnet specimens before and after the corrosion. The potentiodynamic polarization curves of the

magnets in 3.5wt% NaCl solution were obtained by an electrochemical workstation (CHI 660E).

2 Results and Discussion

2.1 Microstructure

According to Fig. 1a and 1b, the magnets after vacuum sintering and low-pressure sintering have similar microstructures. The white Nd-rich phases are distributed at the boundary of the dark gray main phase grains^[16]. However, their morphologies and phase distributions are different. According to Fig. 1c and 1d, the main phase grains of vacuum-sintered magnets have more sharp corners, as indicated by the arrows in Fig. 1c. The main phase grains of low-pressure-sintered magnets are more regular.

Fig.2a and 2b show the grain size distributions of vacuum-sintered and low-pressure-sintered magnets, respectively. It can be seen that the grain size distribution is more concentrated in the low-pressure-sintered magnet, indicating that its grain size is more uniform. The grain size of the vacuum-sintered magnet is mainly 4–6 μm , while that of the low-pressure-sintered magnet is primarily 3–5 μm . The average grain size of the low-pressure-sintered specimen is 4.098 μm , which is smaller than that of the vacuum-sintered specimen (5.043 μm). Therefore, the low-pressure-sintered magnets have uniformly refined main phase grains.

The distribution of Nd-rich phase in the sintered magnets has two forms: the main phase at the triangular grain boundary and the thin-layer phase between the main phase grains. Table 1 shows the area fraction of Nd-rich phase in the sintered magnets. It can be seen that the bulk Nd-rich phase in vacuum-sintered magnets accounts for 3.95%, while that in the low-pressure-sintered magnets decreases to 3.06%. Thus,

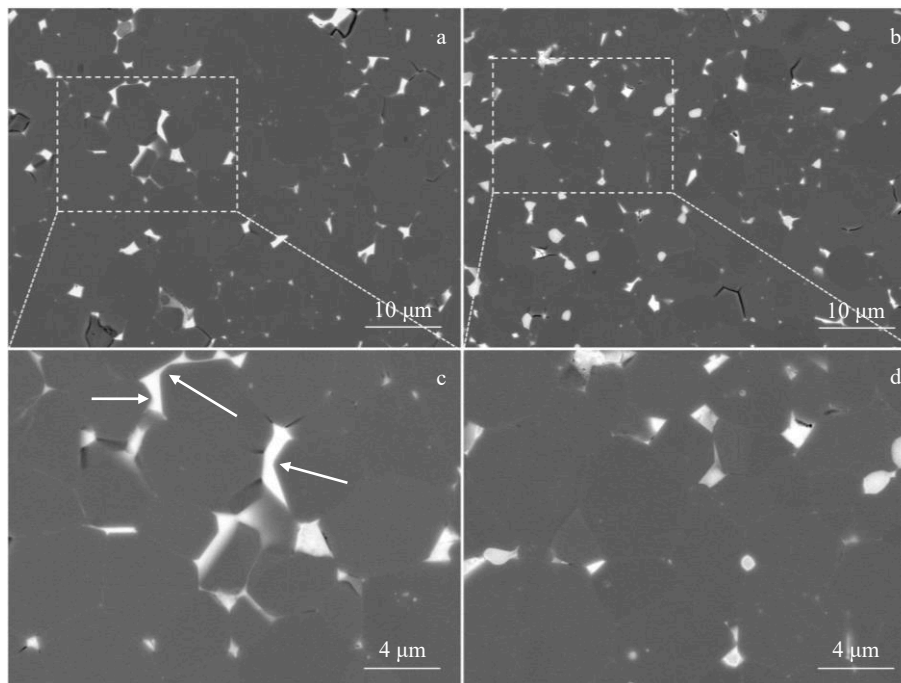


Fig.1 SEM microstructures of vacuum-sintered (a, c) and low-pressure-sintered (b, d) magnets

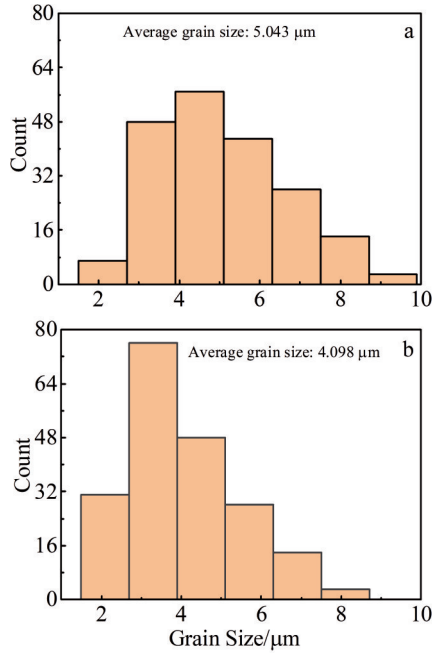


Fig.2 Grain size distribution of vacuum-sintered (a) and low-pressure-sintered (b) magnets

it can be concluded that the low-pressure sintering promotes

the flow of Nd-rich phase: the Nd-rich phase is transferred from the triangular grain boundary to the intergranular phase area of the main phase. The transference of Nd-rich phases reduces the direct contact between main phase grains.

2.2 Thermal stability

Demagnetization curves of the vacuum-sintered and low-pressure-sintered magnets at different temperatures are shown in Fig.3. Compared with that of the vacuum-sintered magnets, the coercivity of low-pressure-sintered magnets at room temperature is increased, which is attributed to the refinement of grains and the improvement of the Nd-rich phase distribution^[17-18]. With increasing the temperature, the coercivity is decreased gradually. The coercivity of low-pressure-sintered magnet is higher than that of the vacuum-sintered magnet at all temperatures. When the temperature rises from 20 °C to 200 °C, the remanence of the vacuum-sintered magnet is decreased from 1.386 T to 1.053 T, whereas that of the low-pressure-sintered magnet is decreased from 1.368 T to 1.043 T. In addition, the coercivity of the vacuum-sintered and low-pressure-sintered magnets is decreased from 1614.290 kA/m to 194.940 kA/m and from 1739.260 kA/m to 262.998 kA/m, respectively. The temperature coefficients of remanence α_{Br} and that of coercivity $\beta_{H_{cj}}$ of different magnets are also shown in Fig.3c and 3d, respectively. The temperature

Table 1 Area fraction of bulk Nd-rich phases in vacuum-sintered and low-pressure-sintered magnets (%)

Magnet	Area fraction of bulk Nd-rich phase					Average area fraction
Vacuum-sintered	3.63	3.70	4.46	3.35	4.63	3.95
Low-pressure-sintered	3.14	3.53	3.61	2.48	2.52	3.06

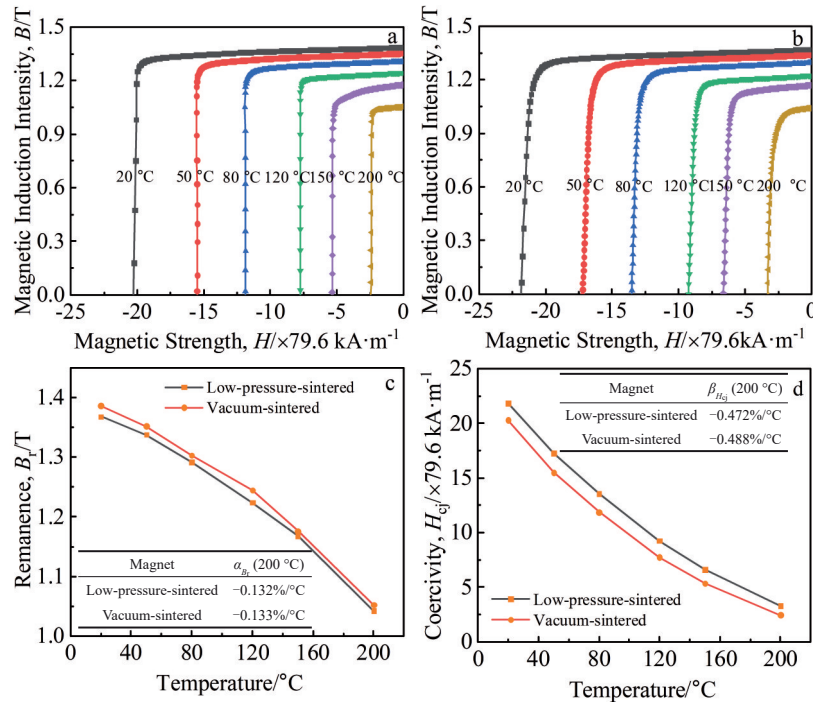


Fig.3 Demagnetization curves of vacuum-sintered (a) and low-pressure-sintered (b) magnets at different temperatures; remanence (c) and coercivity (d) of vacuum-sintered and low-pressure-sintered magnets

coefficients of remanence of vacuum-sintered and low-pressure-sintered magnets are $-0.133\%/^{\circ}\text{C}$ and $-0.132\%/^{\circ}\text{C}$, respectively, which are basically the same. The temperature coefficients of coercivity of vacuum-sintered and low-pressure-sintered magnets are $-0.488\%/^{\circ}\text{C}$ and $-0.472\%/^{\circ}\text{C}$, respectively. It can be seen that the low-pressure-sintered magnets have a smaller temperature coefficient of coercivity, indicating the better thermal stability.

The parameters related to the microstructure in the temperature coefficient of coercivity were introduced to investigate the internal relationship between microstructure changes and temperature stability. The coercivity of sintered NdFeB magnets can be expressed by the phenomenological micromagnetic model^[19], as follows:

$$H_{cj}(T) = \alpha H_a(T) - N_{\text{eff}} M_s(T) \quad (3)$$

where α describes the anisotropic field change caused by the interface defects; N_{eff} represents the variation of the stray field inside the magnet; H_a is the magnetic crystal anisotropy field; M_s is the saturation magnetization of magnets; T is the operating temperature. Combining the temperature coefficient of coercive force and the physical model of coercivity, $\beta_{H_{cj}}$ can be expressed^[10], as follows:

$$\beta_{H_{cj}} = h + \frac{h - m}{\frac{\alpha}{N_{\text{eff}}} k - 1} \quad (4)$$

$$h = \frac{H_a(T_1) - H_a(T_0)}{H_a(T_0)(T_1 - T_0)}$$

$$m = \frac{M_s(T_1) - M_s(T_0)}{M_s(T_0)(T_1 - T_0)}$$

$$k = \frac{H_a(T_0)}{M_s(T_0)}$$

where h and m represent the temperature coefficients of H_a and M_s , respectively; k is the magnetic hardness parameter^[20]. These parameters are related to the intrinsic magnetic properties, and the parameter α and N_{eff} are sensitive to the magnet microstructure^[21].

According to these results, the low-pressure sintering enhances the dissolution precipitation during the liquid phase sintering process, which significantly reduces the number of sharp edges of the main phase grains. The more regular the main phase grains, the smaller the demagnetizing field factor N_{eff} . Besides, the obvious grain refinement phenomenon in the low-pressure-sintered magnet is also beneficial to decrease the demagnetizing field factor N_{eff} . As for the Nd-rich phase distribution, the low-pressure sintering promotes the flow of Nd-rich phase from the triangular grain boundary to the intergranular area of main phases, thereby reducing the number of interfaces between the main phase grains, which leads to the higher structural factor α ^[21-22].

In conclusion, a larger α and a smaller N_{eff} can be obtained due to the microstructure change in the magnets after low-pressure sintering, which results in the larger ratio of α to N_{eff} . Combined with Eq. (4), the larger the ratio of α/N_{eff} , the smaller the $\beta_{H_{cj}}$, therefore the better the thermal stability.

2.3 Salt solution immersion corrosion

The potentiodynamic polarization curves of the vacuum-sintered and low-pressure-sintered magnets are shown in Fig. 4. The Tafel method was used for curve fitting, and the corrosion potential (E_{corr}) and corrosion current density (i_{corr}) are presented in Table 2. Compared with the vacuum-sintered magnet, the low-pressure-sintered magnet has higher corrosion current density, indicating that its corrosion rate is faster in the 3.5wt% NaCl solution. The lower the corrosion potential, the stronger the corrosion tendency. The difference in corrosion resistance may be related to the distribution change of Nd-rich phases in the magnets^[23-24]. The low-pressure sintering promotes the flow of Nd-rich phases from the triangular grain boundary to intergranular area of main phases, resulting in a complete network structure of Nd-rich phases. Increasing the contact area between the cathode (main phase) and anode (Nd-rich phase) is conducive to the formation of more corrosion micro-couples, which aggravates the corrosion of magnet.

Corrosion reaction rates of the magnets are fitted by the Arrhenius equation, as shown in Fig. 5. The relationship between the corrosion mass loss of magnet ΔW and the corrosion rate can be expressed by Eq. (5) and Eq. (6), respectively, as follows:

$$\Delta W^n = kt \quad (5)$$

$$\ln k = -\frac{E_a}{RT} \quad (6)$$

where n is the power exponent; k is the corrosion rate constant; t is corrosion duration; E_a is the activation energy; R is the gas constant. It can be seen that the activation energy E_a of corrosion reaction of low-pressure-sintered and vacuum-sintered magnets is 8.76 and 9.34 $\text{kJ}\cdot\text{mol}^{-1}$, respectively. The low-pressure-sintered magnets have smaller activation energy for corrosion reaction, suggesting the easy occurrence of

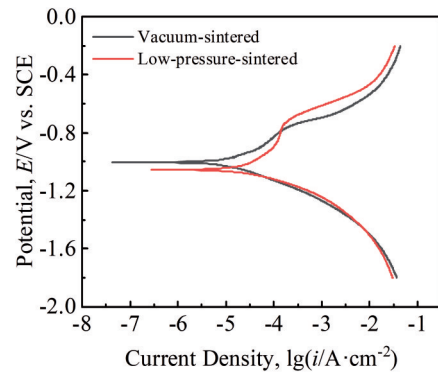


Fig.4 Potentiodynamic polarization curves of vacuum-sintered and low-pressure-sintered magnets in 3.5wt% NaCl solution

Table 2 Corrosion potential E_{corr} and corrosion current density i_{corr} of vacuum-sintered and low-pressure-sintered magnets

Magnet	$E_{\text{corr}}/\text{V vs. Ag/AgCl}$	$i_{\text{corr}}/\times 10^{-5} \text{ A}\cdot\text{cm}^{-2}$
Vacuum-sintered	-1.004	1.191
Low-pressure-sintered	-1.055	2.576

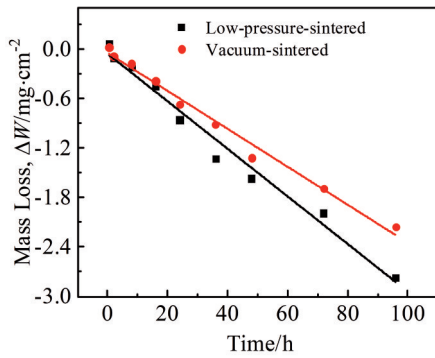


Fig.5 Mass loss fitting lines of vacuum-sintered and low-pressure-sintered magnets in 3.5wt% NaCl solution

corrosion reaction, i.e., the low-pressure-sintered magnet has a stronger corrosion tendency and a fast corrosion rate.

Fig. 6 shows the microstructure change of vacuum-sintered magnets after corrosion in 3.5wt% NaCl solution. During the initial stage of corrosion, the corrosion traces can be preferentially observed at the Nd-rich phase area. Due to its lower corrosion potential, the Nd-rich phase acts as an anode during the corrosion process. The formation of corrosion couples intensifies the unevenness of two-phase corrosion. After immersion in 3.5wt% NaCl solution for 2 h, the corrosion morphology of the vacuum-sintered magnet is shown in Fig.6c. Obvious cracks are observed along the grain boundaries. When the corrosion galvanic couple of a large cathode and a small anode forms on the magnet surface, the corrosion of the Nd-rich phase is significantly intensified. Therefore, after the Nd-rich phase is consumed, some cracks form between the grains of the main phase^[25]. With prolonging the immersion duration to 16 h, the surface layer of the

vacuum-sintered magnet obviously peels off, as shown in Fig. 6d. The main phase begins to exfoliate during the consumption of Nd-rich phase which is around the main phase. Thus, the grains of polygonal main phase remain after the exfoliation along the grain boundaries. Fig.6e presents the surface morphology of vacuum-sintered magnet after corrosion for 48 h. The surface layer completely peels off, and the black holes can be observed on the surface. The corrosion products accumulate in some holes, which promotes the formation of occluded cells, therefore leading to the acidification inside the magnet and resulting in the free hydrogen atoms^[26]. These hydrogen atoms easily combine with the main phase and Nd-rich phase, which aggravates the initiation and development of cracks^[27]. With prolonging the corrosion duration to 96 h, the corrosion morphology of the vacuum-sintered magnet can be observed in Fig. 6f. Many cracks form on the magnet surface, which can be explained by the following reasons. The corrosion couples accelerate the consumption of Nd-rich phase, which leaves cracks between the main phases along the grain boundaries. The occluded cells begin to appear after corrosion for 16 h, as well as the peeling phenomenon. In comparison, the surface layer of low-pressure-sintered magnet completely peels off after corrosion for 16 h. The difference in corrosion behavior of these two magnets is mainly due to the distribution change of Nd-rich phases^[28]. The low-pressure promotes the flow of liquid phases and causes the diffusion of Nd-rich phases from the triangular grain boundary to the intergranular area of main phases, thus forming a more complete network structure which provides a fast diffusion channel for corrosion^[29]. In addition, the complete intergranular Nd-rich phase is also conducive to the cells, which also leads to the acidification of

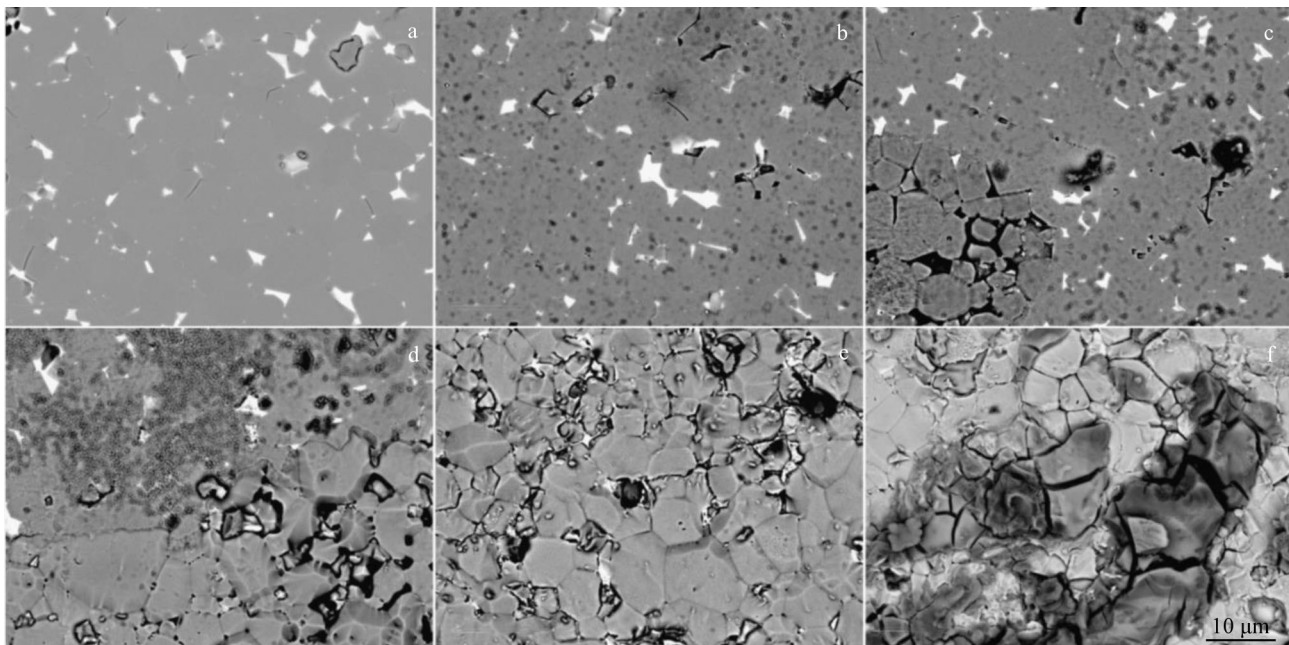


Fig.6 Corrosion morphologies of vacuum-sintered magnets after immersion in 3.5wt% NaCl solution for 0 h (a), 0.5 h (b), 2 h (c), 16 h (d), 48 h (e), and 96 h (f)

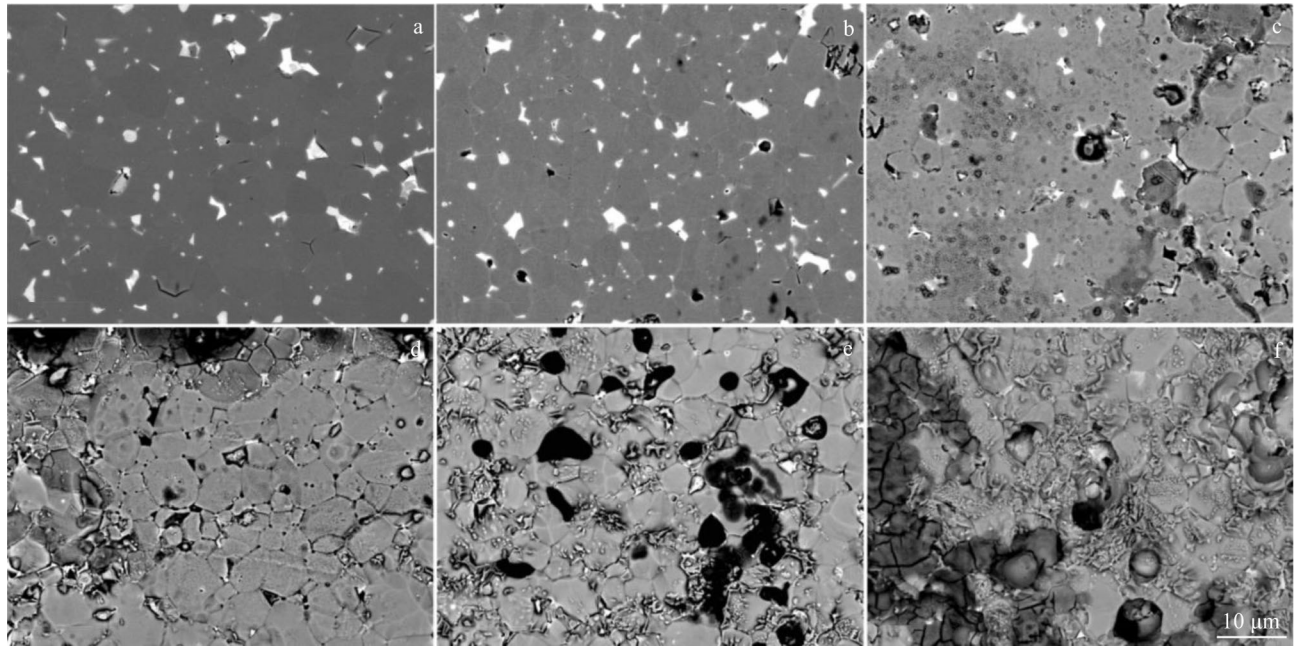


Fig.7 Corrosion morphologies of low-pressure-sintered magnets after immersion in 3.5wt% NaCl solution for 0 h (a), 0.5 h (b), 2 h (c), 16 h (d), 48 h (e), and 96 h (f)

pores and generates the free hydrogen atoms. The combination of hydrogen atoms and constituent phases also accelerates the initiation of cracks. The generated massive black corrosion product has volume expansion effect, which promotes the formation of cracks. Fissures continue to initiate and develop, eventually causing the spalling. The corrosion consumption of the main phase and Nd-rich phase can be observed during the corrosion process. Intergranular exfoliation can also be observed. The corrosion behavior of vacuum-sintered magnets is the region-selective layered spalling.

The corrosion morphologies of low-pressure-sintered magnets are shown in Fig.7. Fig.7b shows the morphology of low-pressure-sintered magnet after corrosion for 0.5 h. In the initial corrosion stage, the corrosion traces are preferentially observed at the Nd-rich phase area. When the immersion duration reaches 2 h, the surface of low-pressure-sintered magnet presents noticeable peeling morphology, as shown in Fig.7c. According to Fig.7d, more corrosion couples form on the magnet surface. Therefore, the low-pressure-sintered magnets show a more severe corrosion tendency. After corrosion for 48 h, a more complete network structure forms in the low-pressure-sintered magnet, which accelerates the corrosion and generates more holes, compared with the vacuum-sintered magnet. These pores are conducive to the formation of occluded cells. Hence, the corrosion rate is further accelerated. As shown in Fig.7f, in addition to the cracks and spalling, the surface of main phase area becomes rough. Compared with that of the vacuum-sintered magnet, in the later corrosion stage, the Nd-rich phase of the low-pressure-sintered magnet is consumed faster, and the galvanic protection effect of the main phase is weakened. Because the

exfoliation of the main phase is aggravated in the low-pressure-sintered magnet, the corrosion consumption of the main phase is also intensified.

3 Conclusions

1) Compared with that of the vacuum-sintered NdFeB magnet, the thermal stability of low-pressure-sintered NdFeB magnet is significantly improved, and the temperature coefficient of coercivity is decreased from $-0.488\%/^{\circ}\text{C}$ to $-0.472\%/^{\circ}\text{C}$. The corrosion resistance of low-pressure-sintered NdFeB magnet also decreases.

2) The low-pressure sintering can obtain refined and regular main phase grains for the NdFeB magnets, which results in the smaller demagnetizing field factor N_{eff} . The uniformly distributed Nd-rich phase reduces the direct contact of main phase grains, which is beneficial to obtain a higher structure factor a . The temperature coefficient of coercivity is negatively correlated to the ratio of a/N_{eff} .

3) Compared with the case in the vacuum-sintered NdFeB magnet, the Nd-rich phase forms a more complete network structure in the low-pressure-sintered magnets, which provides a fast development channel for corrosion, therefore reducing the corrosion resistance of the NdFeB magnets.

References

- 1 Brown D, Ma B M, Chen Z. *Journal of Magnetism and Magnetic Materials*[J], 2002, 248(3): 432
- 2 Sagawa M, Fujimura S, Togawa N et al. *Journal of Applied Physics*[J], 1984, 55(6): 2083
- 3 Gutfleisch O, Willard M, Bruck E et al. *Advanced Materials*[J], 2011, 23(7): 821

- 4 Pandian S, Chandrasekaran V, Markandeyulu G et al. *Journal of Alloys and Compounds*[J], 2004, 364(1-2): 295
- 5 El-Moneim A A, Gebert A, Uhlemann M et al. *Corrosion Science*[J], 2002, 44(8): 1857
- 6 Guan Y W, Huang Y L, Rao Q et al. *Journal of Alloys and Compounds*[J], 2021, 857: 157 606
- 7 Li J J, Guo C J, Zhou T J et al. *Journal of Magnetism and Magnetic Materials*[J], 2018, 454: 215
- 8 Li X B, Liu S, Cao X J et al. *Journal of Magnetism and Magnetic Materials*[J], 2016, 407: 247
- 9 Li J N, Sepehri-Amin H, Sasaki T et al. *Science and Technology of Advanced Materials*[J], 2021, 22(1): 386
- 10 Li R, Zhang H R, Liu Y et al. *Materials Research Express*[J], 2018, 5(5): 56 101
- 11 Sun C, Liu W Q, Sun H et al. *Journal of Materials Science & Technology*[J], 2012, 28(10): 927
- 12 Isotahdon E, Huttunen-Saarivirta E, Kuokkala V T et al. *Materials Chemistry and Physics*[J], 2012, 135(2-3): 762
- 13 Ni Junjie, Wang Yongkang, Jia Zhengfeng et al. *Rare Metal Materials and Engineering*[J], 2016, 45(8): 2111 (in Chinese)
- 14 Li Jiajie, Guo Chengjun, Zhong Minglong et al. *Chinese Rare Earths*[J], 2015, 36(5): 49 (in Chinese)
- 15 Zhao W, Liu Y, Li J et al. *Journal of Materials Processing Technology*[J], 2021, 294: 117 110
- 16 Vial F, Joly F, Nevalainen E et al. *Journal of Magnetism and Magnetic Materials*[J], 2002, 242-245(2): 1329
- 17 Woodcock T G, Zhang Y, Hrkac G et al. *Scripta Materialia*[J], 2012, 67(6): 536
- 18 Ramesh R, Thomas G, Ma B M. *Journal of Applied Physics*[J], 1988, 64(11): 6416
- 19 Kronmüller H. *Physica Status Solidi B*[J], 1987, 144(1): 385
- 20 Skomski R, Coey J M D. *Scripta Materialia*[J], 2016, 112: 3
- 21 Kronmüller H. *Supermagnets, Hard Magnetic Materials*[M]. Dordrecht: Springer, 1991: 461
- 22 Grönefeld M, Kronmüller H. *Journal of Magnetism and Magnetic Materials*[J], 1989, 80(2-3): 223
- 23 Liu Y L, Liang J, He Y C et al. *AIP Advances*[J], 2018, 8(5): 56 227
- 24 Yu L Q, Wen Y H, Yan M. *Journal of Magnetism and Magnetic Materials*[J], 2004, 283(2-3): 353
- 25 Li Hongying, Hao Zhuangzhi, Liu Yuhui et al. *Rare Metal Materials and Engineering*[J], 2018, 47(5): 1451 (in Chinese)
- 26 Brown B F. *Corrosion*[J], 1970, 26(8): 349
- 27 Luo J J, De Rango P, Fruchart D et al. *Journal of Alloys and Compounds*[J], 2011, 509(11): 4252
- 28 Liu Weiqiang, Yue Ming, Zhang Jiuxing et al. *Rare Metal Materials and Engineering*[J], 2007, 36(6): 1066 (in Chinese)
- 29 Riposan I, Chisamera M. *Giessereitechnik*[J], 1988, 34(3): 86

低压烧结对NdFeB磁体微观结构与服役稳定性的影响

赵常宇, 刘颖, 赵伟, 侯贺楠, 李军
(四川大学材料科学与工程学院, 四川成都 610065)

摘要: 研究了NdFeB磁体微观结构和服役稳定性的内在联系。结果表明, 低压烧结NdFeB磁体具有更加细小的晶粒尺寸和分布更为均匀的晶间富钕相, 有利于磁体获得更小的矫顽力温度系数, 从而提高其温度稳定性。对比真空烧结后的磁体, 低压烧结磁体的矫顽力温度系数从-0.488%/°C减小至-0.472%/°C。但是富钕相从三角晶界向主相晶间流动形成了完整的网状结构, 不利于磁体的耐腐蚀性能。低压烧结磁体在3.5% (质量分数) NaCl溶液中浸泡后腐蚀失重更为严重, 表现出更强的腐蚀倾向。

关键词: 低压烧结NdFeB磁体; 微观结构; 温度稳定性; 耐腐蚀性能

作者简介: 赵常宇, 男, 1997年生, 硕士, 四川大学材料科学与工程学院, 四川成都 610065, E-mail: 1319692675@qq.com